

Full length article

Grain-boundary character distribution and correlations with electrical and optoelectronic properties of CuInSe₂ thin films

Daniel Abou-Ras^{a,*}, Norbert Schäfer^a, Thorsten Rissom^a, Madeleine N. Kelly^b, Jakob Haarstrich^c, Carsten Ronning^c, Gregory S. Rohrer^b, Anthony D. Rollett^b

^a Helmholtz-Zentrum Berlin für Materialien und Energie GmbH, Hahn-Meitner-Platz 1, 14109 Berlin, Germany

^b Department of Materials Science and Engineering, Carnegie Mellon University, 5000 Forbes Avenue, Pittsburgh, PA 15213, USA

^c Institut für Festkörperphysik, Friedrich-Schiller-Universität Jena, Max-Wien-Platz 1, 07743 Jena, Germany

ARTICLE INFO

Article history:

Received 21 April 2016

Received in revised form

18 July 2016

Accepted 21 July 2016

Keywords:

Grain-boundary character distribution

CuInSe₂ thin films

EBSD

EBIC

CL

ABSTRACT

Thin-film solar cells based on polycrystalline Cu(In,Ga)Se₂ absorbers exhibit record conversion efficiencies of up to 22.6%. There is still a lack of a quantitative connection between the grain-boundary character distribution (GBCD) and the corresponding electrical and optoelectronic properties. The present work uses microstructural data from a CuInSe₂ thin film acquired by electron backscatter diffraction (EBSD) to evaluate the GBCD. The most prominent features of the GBCD of CuInSe₂ are Σ3 twin boundaries and the Σ9 and Σ27a symmetric tilt grain boundaries. Moreover, combining EBSD with electron-beam-induced current and cathodoluminescence (measurements on the same identical area) on a CuInSe₂/Mo/glass stack provide the means to relate the grain-boundary character with the corresponding electrical and optoelectronic signals across the grain boundary. In part, determining this relationship is accomplished by means of correlation analysis using measurement data from more than 100 grain boundaries. However, the crystallographic, electrical and optoelectronic data showed no strong correlations, which is attributed to atomic reconstruction found in atomic planes adjacent to planar defects in polycrystalline CuInSe₂ thin films and corresponding reductions of excess charge densities at these defects.

© 2016 Acta Materialia Inc. Published by Elsevier Ltd. All rights reserved.

1. Introduction

Thin-film solar cells based on Cu(In,Ga)Se₂ absorbers exhibit record conversion efficiencies of up to 22.6% [1]. Cu(In,Ga)Se₂ thin films are polycrystalline and have average grain sizes of about 0.5 μm at film thicknesses of 2–3 μm (for the Cu(In,Ga)Se₂ record devices) [2]. Copious scientific work has already been dedicated to elucidate the microstructural origins for the outstanding device performance (see reviews in Refs. [3,4]). When investigating only a few random grain boundaries on a cross-sectional specimen of a Cu(In,Ga)Se₂ solar cell, the local short-circuit current measured by electron-beam-induced current (EBIC) analysis exhibited only slight reductions of 5–10% at the positions of the grain boundaries, with recombination velocities determined to about 10³–10⁴ cm/s [5]. Moreover, the radiative recombination probed locally by cathodoluminescence (CL) images has been found to be reduced

considerably at random grain boundaries [6]. In contrast, no substantial changes of either EBIC or CL signals have been detected at (most) twin boundaries in Cu(In,Ga)Se₂ thin films [5,6].

In spite of the reports already available in the literature (reviewed by Refs. [3,4]), there is still a lack of a detailed, microstructural analysis of grain-boundary properties correlated with corresponding electrical and optoelectronic characterization, which is based on a sufficiently large number of grain-boundaries to provide good statistics. It is noteworthy that a statistical evaluation of results from correlative structural, electrical, and optoelectrical characterization of grain boundaries is not even available for well-studied semiconductor materials such as multicrystalline Si (e.g., Ref. [7]).

The present work deals with the assessment of grain-boundary character distributions (GBCDs) by the evaluation of microstructural data from a CuInSe₂ thin film acquired by electron backscatter diffraction (EBSD). CuInSe₂ thin films, which do not exhibit any compositional gradients of the matrix elements, in contrast to Cu(In,Ga)Se₂ layers (that have considerable In/Ga gradients

* Corresponding author.

E-mail address: daniel.abou-ras@helmholtz-berlin.de (D. Abou-Ras).

perpendicular to the substrate) were chosen for the present study in order to avoid corresponding influences on the EBSD measurements. Moreover, combined EBSD with EBIC and CL measurements on the same identical area of a $\text{CuInSe}_2/\text{Mo}/\text{glass}$ stack provide the means to relate the grain-boundary type with the corresponding electrical and optoelectronic signals across each grain boundary.

2. Experimental details

The $\text{CuInSe}_2/\text{Mo}/\text{glass}$ stacks were fabricated by co-evaporation of about 2 μm thick CuInSe_2 thin films on Mo-coated glass substrates. Details of this process are published elsewhere [8]. A part of this stack was further processed to complete solar cells by the deposition of a CdS buffer and a $\text{ZnO:Al}/\text{i-ZnO}$ bilayer as front contact. These solar cells reached conversion efficiencies of about 12–13%. After deposition of a graphite layer (serving as diffusion barrier for Ag in the epoxy glue) on the $\text{i-ZnO}/\text{ZnO:Al}$ front contact, the solar-cell stack was glued by use of Ag epoxy glue to an Al sample holder. The backside of the Cu(In,Ga)Se_2 absorber layer was exposed by lifting off the Mo-coated glass substrate. In order to passivate the CuInSe_2 (back) surface and to enhance the conductivity, a graphite layer (nominal thickness of 4–5 nm) was evaporated on top.

The EBSD and EBIC analyses were conducted using a Zeiss UltraPlus™ scanning electron microscope, equipped with an Oxford Instruments NordlysNano™ EBSD camera and an EBIC amplifier by Point Electronic GmbH. The EBSD maps were acquired at 15 kV and 55 nA by means of the AZtec software suite. In the present analysis, the tetragonal chalcopyrite structure of CuInSe_2 was assumed to be the cubic sphalerite structure; i.e., we use in what follows {111} (cubic) instead of {112} (tetragonal). This is because the chalcopyrite structure can be visualized as two sphalerite units stacked along the c axis. Because the ratio of the tetragonal lattice constants, c/a , deviates only slightly from 2 (about 0.2% [9]), the diffraction is not sufficiently different from the cubic structure to be distinguished in a high-rate EBSD experiment.

The reconstructed grain boundary line segments for the stereological GBCD calculation were extracted from the cleaned up EBSD maps using the TSL/OIM™ software. In this process, the grain boundary positions are first approximated as straight lines connecting all of the triple junctions. If these line segments deviate by more than two pixels from the actual grain boundary position on the map, the segments are subdivided to match the path of the grain boundary to within the required precision [10]. The procedure resulted in more than 136,000 grain boundary line segments. The procedures used to calculate the grain boundary character distribution from these line segments are described elsewhere [11,12] and have been applied to many other materials in the past [13–21]. All calculations were carried out under the assumption of cubic symmetry using Fortran programs [22].

The beam energy and the beam current for the EBIC measurements, 8 kV and 100 pA, were kept low, in order to provide good spatial resolutions on the one hand and to avoid high-injection conditions at the same time. Further details on the EBIC measurements are described in a previous report [23].

CL images were obtained at 8 kV and 250 pA using a JEOL SEM 6490 microscope and a Gatan monoCL3 system with a monochromator and an (In,Ga)As photomultiplier Hamamatsu R5509-73, which was cooled to 193 K. The sample was placed on a liquid-He-cooled cryo-stage, leading to sample temperatures of about 8 K. From the EBIC and CL images, profiles were extracted across grain boundaries, which were located and categorized by means of the EBSD maps. The profiles used for the evaluation of the EBIC and CL signals are averages of each 15 individual profiles across the grain boundaries.

Pairs of (sets of Bunge) Euler angles were analyzed to obtain the angle of disorientation (i.e., misorientation with minimum rotation angle), the Rodrigues vector of each disorientation, the scalar product between the rotation axis and $\langle 100 \rangle$, $\langle 110 \rangle$ and $\langle 111 \rangle$ axes (normalized), as well as the three components of the disorientation axis expressed in the sample frame. Canonical correlation analysis (CCA) [24,25], which is a variant of the much better known principal component analysis (PCA) [26], was used to analyze the aforementioned data. In brief, the CCA aims to identify linear combinations of variables that maximize the cross-correlation between the variables. It differs from PCA in that the variables are split into two groups, an “input” group (“predictor set”) and an “output” group (“criterion set”), and covariance matrices are constructed within each group and between the two groups. Product matrices are then combined together in a block form and an eigenanalysis is performed. The square roots of the corresponding eigenvalues are the canonical correlations and the associated eigenvectors provide the coefficients of the canonical variates, along with canonical loadings from the correlation matrix. The first pair of canonical variates is always chosen to explain the largest part of the variance in the data, i.e. is most predictive. The correlation between an observed variable and the corresponding synthetic variable is known as a structure coefficient (or *loading*). Squared canonical structure coefficients indicate the proportion of variance shared by an observed variable with the associated canonical variate and can be used to decide the relative importance of the variables. The idea behind quantifying the disorientation axis against the 3 basic directions was to check whether or not either electrical signal was correlated with the axis itself. The idea behind including the sample-frame disorientation axis was, specifically for the twin boundaries, to test whether the inclination of the boundary was significant; e.g., a twin boundary oriented perpendicular to the surface must have its common $\langle 111 \rangle$ axis lying in the section plane.

Misorientations were computed in the standard fashion [27] using $\Delta g = \{O\}g_{A|B}g_{B|A}^{-1}\{O\}$, where O signifies the group of (cubic) symmetry operators and g represents the orientation [28] adjacent to a boundary. The particular choice of operator and \overline{AB} versus \overline{BA} is governed by identifying the disorientation, i.e., locating Δg in a fundamental zone. Proximity to a given axis was computed as the magnitude of the dot product between the axis (as a unit vector) and the misorientation axis (as a unit vector). The misorientation axis in the sample frame was computed from the skew-symmetric part of $g_{A|B}^{-1}g_{B|A}$, normalized to make it a unit vector. The output of the analysis was used as input for the CCA and all the quantities associated with grain boundaries were regarded as input variables. Version 3.2.1 of the R software suite [29], with the *car* and *yacca* packages [30], was used to perform the CCA and to plot the results. The EBIC and CL weights were assigned as the “output” variables for the CCA, according to the procedures described in Refs. [24,25].

3. Results and discussions

3.1. Grain-boundary character distribution

For all grain boundary line segments in the EBSD map (Fig. 1), which was acquired on the $\text{CuInSe}_2/\text{Mo}/\text{glass}$ stack, the disorientation was calculated and discretized in bins with a 1° width (using the program *disor*) [22]. The results are illustrated in Fig. 2 and compared with a random distribution [31]. Note that a disorientation cut-off of 5° was used to define grains in the clean-up procedure, i.e., the values below 5° are zero. Overall, the disorientation angle distribution follows the same trend as the random distribution, except for three noticeable peaks, which are located at 32° , 39° , and 60° .

To learn more about the boundaries that make up these local

maxima, the distribution of disorientation axes was computed at these three disorientation angles. The calculation was carried out (Fortran program `graph_ax_ang` [22]) using eleven discrete bins per 90° of misorientation space, or a resolution of about 8.2° . The results, shown in Fig. 3, illustrate the distribution of disorientation axes at these angles. In each case, the distribution peaks at a low index direction, indicating that the majority of the grain boundaries have this disorientation axis. The units are in multiples of a random distribution (MRD), which is a measure of the fractional length of such boundaries divided by the fractional length that would be expected in a random distribution of grain boundaries. At 32° , at 39° , and at 60° , the maxima are at $[101]$, at $[101]$, and at $[111]$. In the coincident-site lattice terminology [32], these are $\Sigma 27a$, $\Sigma 9$, and $\Sigma 3$ grain boundaries (see Fig. 4).

We consider the distribution of grain boundary planes at these disorientations, because there are local maxima in the grain boundary population at $\Sigma 27a$, $\Sigma 9$, and $\Sigma 3$. The grain-boundary character distribution was calculated with the same resolution as the axis-angle distribution (Fortran program `graph_gbcd`) [22]. The distribution of grain boundary planes for the $\Sigma 27a$ boundaries is maximized along the zone of tilt boundaries (those boundary plane orientations which are perpendicular to the $[110]$ disorientation axis). The distribution maximizes at the $[1\bar{1}5]$ orientation, which is consistent with the orientation of one of the symmetric tilt boundary. The other symmetric tilt in this distribution, at $(\bar{5}52)$, is a minimum of the distribution. The distribution of grain boundary planes for the $\Sigma 9$ boundary is similar: most boundaries have tilt character and the distribution maximizes at the position of the $(1\bar{1}4)$ symmetric tilt. One important difference is that the population of the $\Sigma 9$ symmetric tilt boundaries (68 MRD) is significantly larger than the $\Sigma 27a$ symmetric tilt boundaries (8 MRD). The distribution of grain boundary planes for the $\Sigma 3$ boundary is strongly peaked at the (111) positions, i.e., the grain boundary planes are perpendicular to the $[111]$ disorientation axis and they are twist boundaries. This corresponds to the common twin-boundary configuration found in many cubic materials [33]. Boundaries with this character make up about one quarter of all of the boundaries in the CuInSe_2 thin film.

The most prominent features of the grain boundary character distribution of CuInSe_2 are the twin boundaries ($60^\circ/[111]$) and the $\Sigma 9$ and $\Sigma 27a$ symmetric tilt grain boundaries. It is very likely that the $\Sigma 9$ and $\Sigma 27a$ boundaries are a geometric consequence of the high concentration of $\Sigma 3$ boundaries. For any triple line where two $\Sigma 3$ grain boundaries meet, there must be a $\Sigma 9$ boundary [34]. We can estimate how many would be formed in this way if we assume

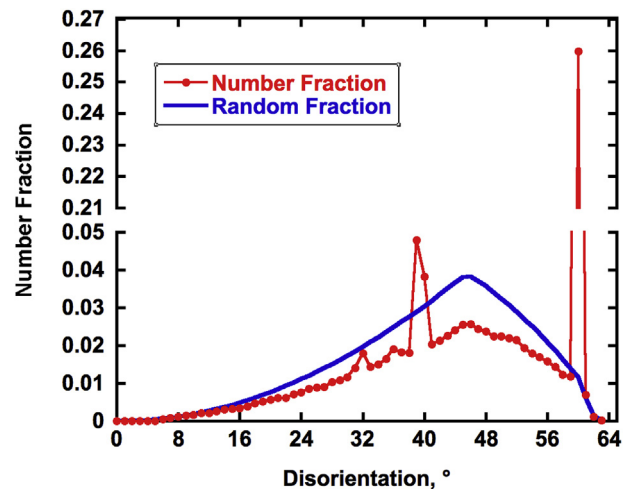


Fig. 2. The disorientation angle distribution for CuInSe_2 , computed with 1° resolution (red circles). The distribution of disorientation angles for a randomly oriented cubic material is included for comparison (blue line). (For interpretation of the references to color in this figure legend, the reader is referred to the web version of this article.)

that triple junctions are constructed by randomly sampling the distribution of disorientations. If so, the probability of choosing two $\Sigma 3$ boundaries and producing a $\Sigma 9$ is $(0.26)^2 = 0.068$; the measured number fraction of $\Sigma 9$ boundaries is 0.05.

Similarly, when a $\Sigma 9$ and $\Sigma 3$ meet, they produce a $\Sigma 27a$. The probability of this occurring is $0.26 \times 0.05 = 0.013$; the measured number fraction of $\Sigma 27a$ boundaries is 0.018. When comparing the estimates with the measured numbers, it should be noted that the measured number fractions are influenced strongly by the exact bin positions. Considering this fact, the similarity of the estimates from random combinations and the measured fractions suggest that many of the $\Sigma 9$ and $\Sigma 27a$ boundaries are a consequence of the high concentration of $\Sigma 3$ boundaries.

The material with the most similar structure that has been studied is Si, with the diamond cubic structure [21]. Multicrystalline Si has also been found to exhibit a high concentration of $\Sigma 3$ twin boundaries and $\Sigma 9$ boundaries, but $\Sigma 27a$ boundaries were not detected in significant concentrations; by contrast, the local maxima in the disorientation angle distribution in multicrystalline Si were assigned to $\Sigma 5$, $\Sigma 11$, and $\Sigma 29a$ boundaries [21]. Furthermore, the $\Sigma 9$ grain-boundary plane distributions in CuInSe_2 and Si are very different. In Si, the maximum is at the $(\bar{2}21)$ symmetric tilt

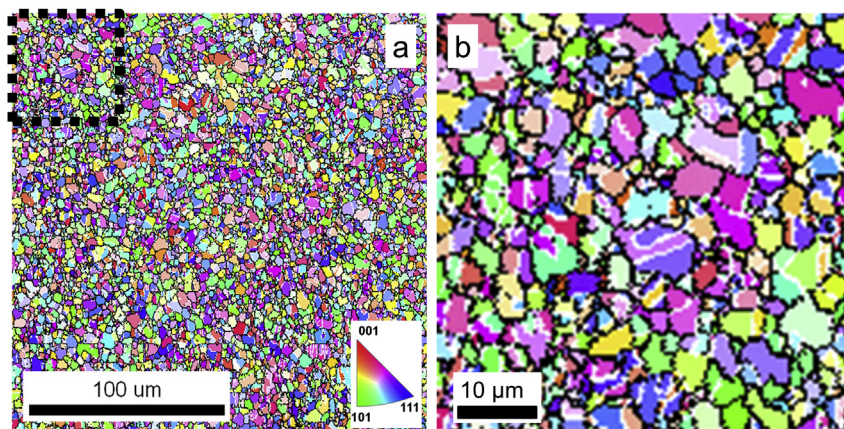


Fig. 1. a) Plan-view EBSD orientation-distribution map of the CuInSe_2 thin film, on which the GBCD is based. The local orientations are given by false colors (see legend). $\Sigma 3$ twin boundaries are highlighted by white lines. b) Magnified section of the EBSD map from the position highlighted by a dotted black square in a). (For interpretation of the references to color in this figure legend, the reader is referred to the web version of this article.)

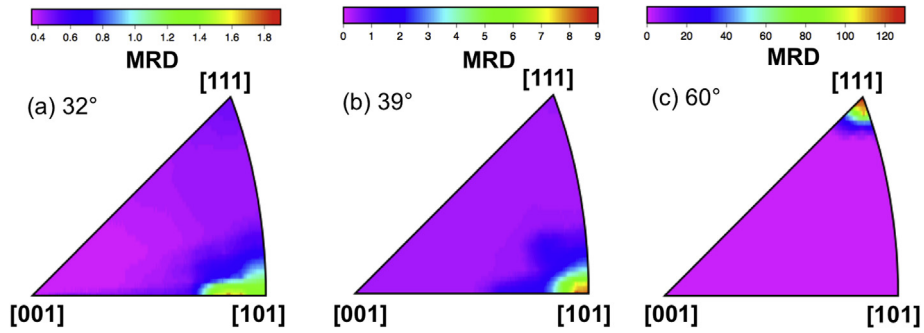


Fig. 3. The distribution of disorientation axes at the disorientation angles of (a) 32°, (b) 39°, and (c) 60°, corresponding to $\Sigma 27a$, $\Sigma 9$, and $\Sigma 3$ grain boundaries. The distribution is plotted in a standard stereographic projection, and the units are multiples of a random distribution.

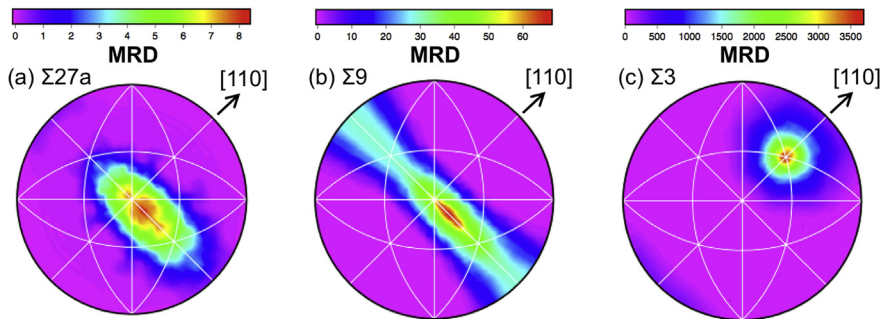


Fig. 4. Grain boundary plane distributions at fixed disorientations. (a) 31.6°/[110], (b) 38.9°/[110], and (c) 60°/[111]. The distributions are plotted on stereographic projections and the [110] direction is in the plane of the page, denoted by the arrow.

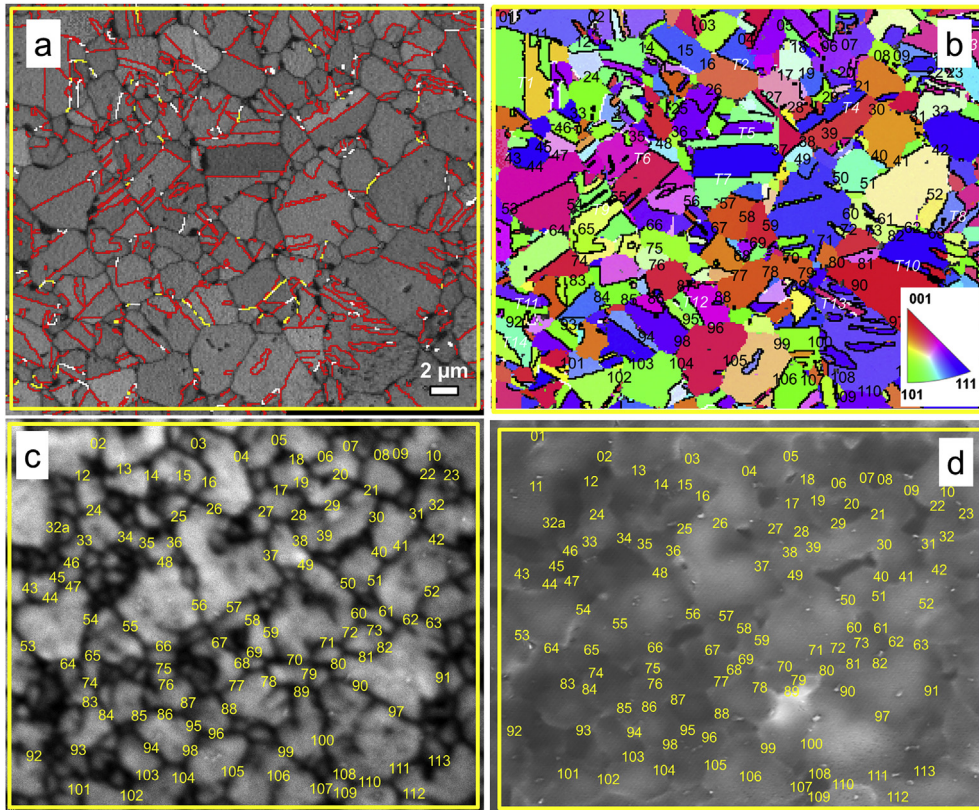


Fig. 5. (a) EBSD pattern-quality maps with $\Sigma 3$, $\Sigma 9$, and $\Sigma 27a$ twin boundaries highlighted by red, white, and yellow lines. (b) EBSD orientation-distribution map with $\Sigma 3$, $\Sigma 9$, and $\Sigma 27a$ twin boundaries highlighted by black, white, and yellow lines. The local orientations are given by false colors (see legend). Selected random grain and $\Sigma 3$ twin boundaries are indexed by black and white numbers. (c) Monochromatic CL image, acquired at 1280 nm, 5 K, and 8 kV. (d) EBIC image, acquired at 8 kV and room temperature. In (c) and (d), selected random grain boundaries are indexed by yellow numbers. (For interpretation of the references to color in this figure legend, the reader is referred to the web version of this article.)

orientation and in CuInSe_2 , it is at the $(\bar{1}\bar{1}4)$ symmetric tilt. It is not too surprising that CuInSe_2 with three different atom types in the crystal structure prefers different interfaces than Si. The added constraint of creating feasible atomic coordinations between unlike atoms at the grain boundaries may be a factor that contributes to the selection of the most common grain boundary structures.

In materials for which grain boundary energies have been measured or calculated, it has been found that the grain boundary plane distribution is inversely correlated to the grain boundary energies, at least in cases where the microstructure has undergone some normal grain growth [35]. Therefore, one may assume that the most highly populated grain boundaries are also the lowest in energy. For the $\Sigma 3$ twin grain boundary in CuInSe_2 with $\{111\}$ twin plane, this would seem to be a safe assumption. In fact, the calculated energy of this boundary is about 0.03 J/m^2 [36], which is similar to the values published for multicrystalline Si [21].

In contrast, the results for the $\Sigma 9$ and $\Sigma 27a$ grain boundaries have to be interpreted with caution. As discussed above, the disorientations of these boundaries are probably a geometric consequence of the high concentration of $\Sigma 3$ boundaries and might not be linked to the average energy of these disorientations. However, among possible boundaries with these disorientations, the preference for $(\bar{1}\bar{1}4)$ and $(\bar{1}\bar{1}5)$ symmetric tilt configurations for the $\Sigma 9$ and $\Sigma 27a$ boundaries is a strong indicator that these are the lowest energy grain boundaries for these disorientations.

3.2. Correlation of structural grain-boundary properties with electrical and optoelectronic signal changes across grain boundaries

3.2.1. Evaluation of EBIC and CL signals across various grain boundaries

In order to correlate directly structural with electrical and optoelectronic properties of individual grain boundaries, EBSD, EBIC, and CL data acquired at the same identical position on the back surface of a $\text{CuInSe}_2/\text{CdS}/\text{ZnO}$ stack (Fig. 5) were evaluated. All grain boundaries were localized by the zero-solutions in the EBSD maps and transferred to the EBIC and CL images via superposition of EBSD map and EBIC/CL images. In contrast to a recent report [23], which treats this (same identical) EBSD/EBIC/CL dataset rather qualitatively, in the present work, EBIC and CL profiles were extracted across 113 random and 14 $\Sigma 3$ twin boundaries (indexed in Fig. 5).

All CL profiles across the selected random grain boundaries exhibit a local minimum at the position of the grain boundary (see Fig. 6 for an example), which is also the case for most (95%) EBIC profiles (see Fig. 7 for an overview). This behavior can be attributed to enhanced, nonradiative recombination via defect states at grain boundaries. The steps visible in some of the EBIC profiles (also present in some of the CL signals) are due to substantially varying EBIC (and CL) signals in neighboring CuInSe_2 grains [6,23] (in some cases, even in different regions within the same grain), which can be attributed to different hole densities [37], affecting both collection (EBIC) and radiative recombination (CL).

All CL profiles and those EBIC profiles which exhibit a local minimum were modeled successfully by using the approaches described in Refs. [23,38]. The average recombination velocities determined at about 100 random grain boundaries by this simulation were for the CL and also the EBIC measurements consistently about $0.5\text{--}2 \times 10^4 \text{ cm/s}$, which can be considered to be rather small values and agree well with values given in earlier reports [5,39]. Local maxima in EBIC profiles across grain boundaries, as the ones detected at two random grain boundaries in the analyzed CuInSe_2 layer (Fig. 7b), have been reported also for n -type Ge in Au/Ge Schottky barriers by Tabet et al. [40]. These authors attributed the increased EBIC signals at grain boundaries to passivation in Ge involving Sb impurities.

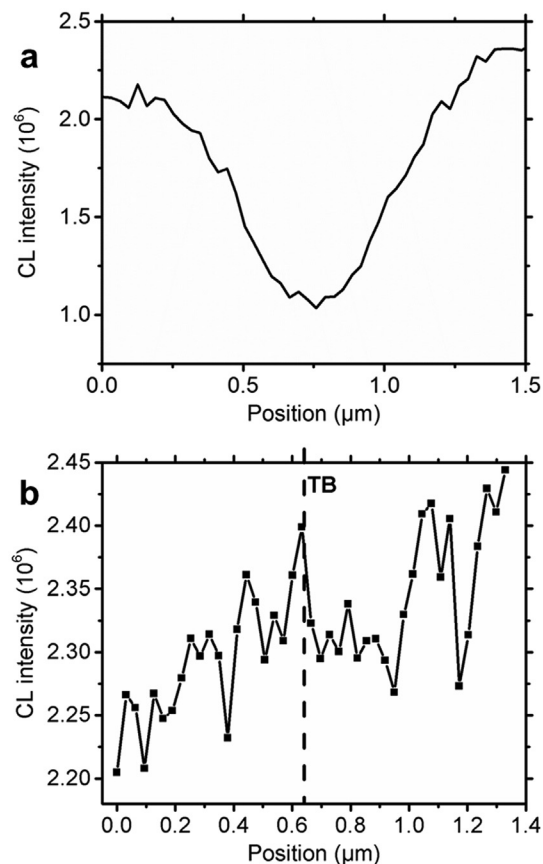


Fig. 6. Profiles (a) across a random grain boundary and (b) across a $\Sigma 3$ twin boundary (TB), both extracted from the CL image in Fig. 5c. The grain boundary in (a) is positioned at the local minimum of the profile, while the position of the TB is indicated by the dashed line in (b), as determined from EBSD map acquired at the same identical position (Fig. 5a).

For the present case of polycrystalline CuInSe_2 thin films, a geometric origin for enhanced EBIC signals at random grain boundaries may also be possible. These thin films are known to exhibit roughnesses ranging from few tens of nm up to few hundreds of nm (depending on the growth recipe applied), forming troughs at the positions of grain boundaries. Therefore, assuming similar widths of the space-charge region for grain interiors and grain boundaries, as well as grain boundaries oriented perpendicular to the substrate, the collection along a grain boundary may be more effective than in the grain interior, and hence the EBIC value is larger. Whether or not a maximum in the EBIC signal is measured may depend on whether the recombination activity at the corresponding grain boundary is substantially larger than in the grain interior.

In contrast to random grain boundaries, EBIC and CL signals at most $\Sigma 3$ twin boundaries do not exhibit a strong impact on the short-circuit current or the radiative recombination (Figs. 6b and 7g). This is also the case for the few $\Sigma 9$ twin boundaries detected in Fig. 5a (see Fig. 8). In contrast, $\Sigma 27a$ boundaries (Fig. 9) show a similar behavior to that observed for random grain boundaries.

Fig. 10 gives the resulting statistics concerning the contrasts of these profiles, which was determined with respect to the lowest signal level measured in the grain adjacent to the twin or grain boundary. Apparently, the CL contrast at most GBs (40–60% of the maximum value) is smaller than the EBIC contrast (80–100% at most random grain boundaries), which can be traced back to the fact that CL was conducted at 8 K, whereas EBIC was performed at room temperature.

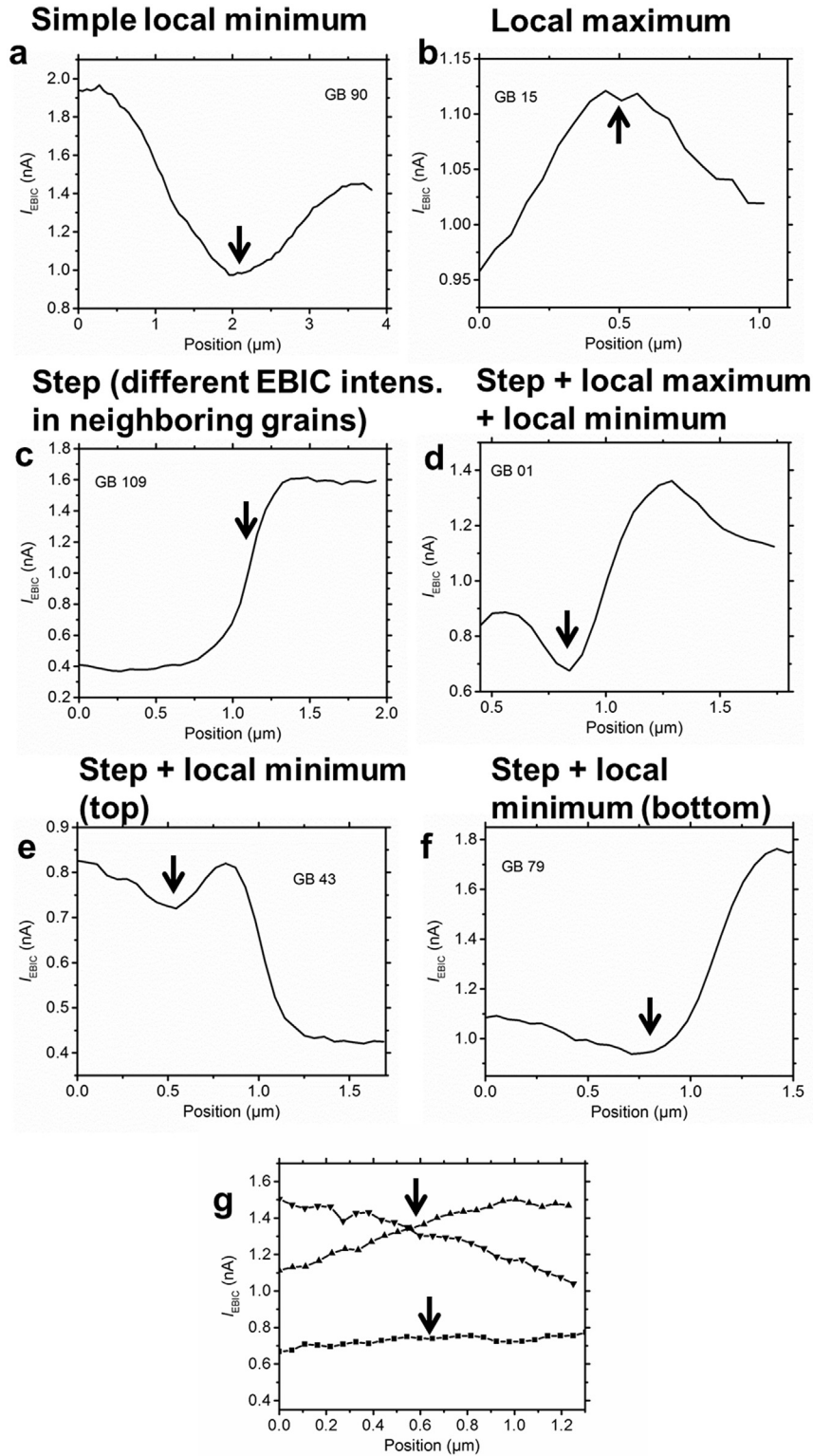


Fig. 7. Profiles extracted across various grain boundaries in the EBIC image in Fig. 5d. The correlation with the EBSD data showed that the grain boundaries are positioned at the local minima (or maximum) of the EBIC profiles in (a)–(f) (highlighted by arrows in the viewgraphs). The steps in the profiles can be explained by differences in the local doping of neighboring grains or, at times, even of regions within individual grains (see Ref. 37). EBIC profiles across various $\Sigma 3$ twin boundaries are given in (g), where the positions of the twin boundaries are indicated by arrows.

The differences between $\Sigma 3$ twin and random grain boundaries can be explained by the much smaller (expected) density of dangling bonds at the twin interfaces. For a few twin boundaries, substantially smaller CL contrasts were detected. For these twins, it

can be expected that the twin planes deviate slightly from the symmetry planes, increasing the densities of dangling bonds and correspondingly enhancing nonradiative recombination.

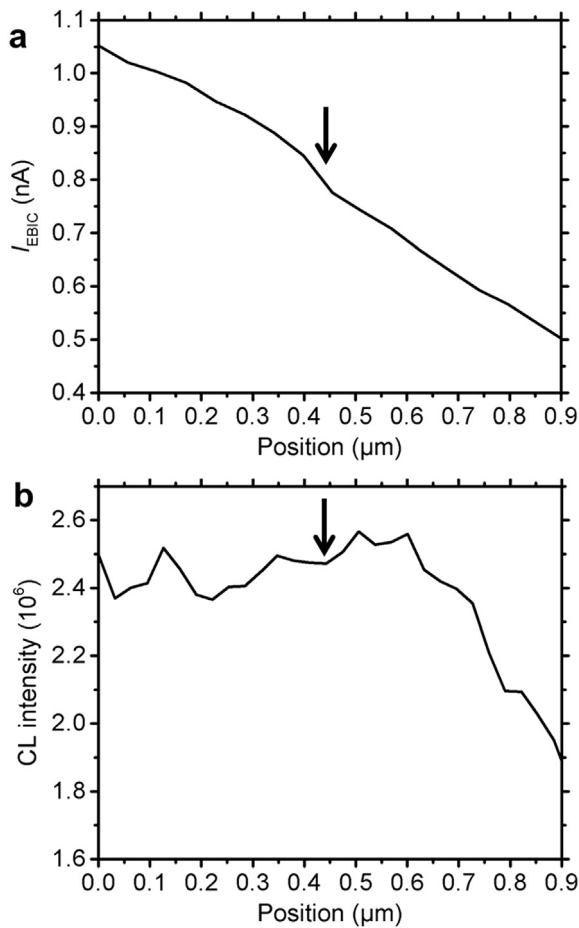


Fig. 8. Profiles extracted across a $\Sigma 9$ twin boundary from the (a) EBIC and (b) CL images in Fig. 5(c) and (d). The position of the $\Sigma 9$ twin boundary is highlighted by arrows. The decrease visible in the CL signal (b) for larger position values (in the region of 0.6–0.9 μm) is due to a random grain boundary in the vicinity.

3.2.2. Results from canonical correlation analysis results

Using the EBSD, EBIC, and CL data from 111 random grain boundaries (two less than the 113 shown above because of incomplete values in the data file) and 14 twin boundaries (total of 125 boundaries) in the studied CuInSe_2 thin film, a statistical analysis was performed to reveal possible correlations between the crystallographic properties and the EBIC and CL signals at these planar defects. Specifically canonical correlation analysis (CCA) was used, for which the data was divided into output variables, namely the CL and EBIC signals, and input variables, namely various quantities related to grain boundary character. The output versus the input for the first pair of canonical variates is shown in Fig. 11, and the equivalent plot for the second pair in Fig. 12. The coefficients and loadings for the input group of variables, as well as the coefficients and loadings for the output group of variables are given in Tables 1 and 2. The CCA showed that a reduction in the complexity of the variables is possible. The output canonical variates, “Y Canonical Variate 1|2”, are combinations of CL (strong loading) and EBIC (weak loading) where CV1 is dominated by the CL signal and CV2 is largely the EBIC signal. The input variates, “X Canonical Variate 1|2”, combine disorientation angle (*angle1*), the three Rodrigues vector components (*rf1*, *rf2*, *rf3*) and the measures of closeness to 100 (*near100*), 110 (*near110*) and 111 (*near111*). Note that the range of all input variables is of order unity except for the disorientation angle (*angle1*), which ranges up to approximately

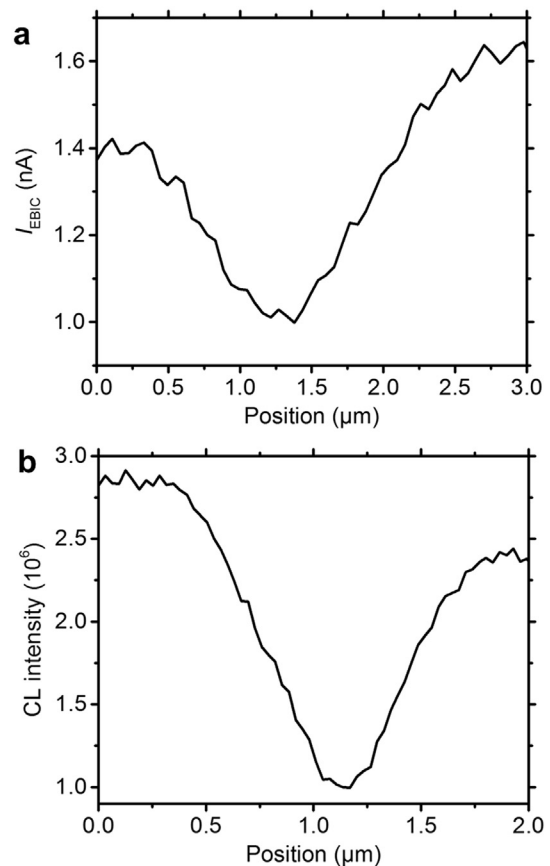


Fig. 9. Profiles extracted across a $\Sigma 27a$ boundary from the (a) EBIC and (b) CL images in Fig. 5(c) and (d). The position of the $\Sigma 27a$ boundary is located at the local minimum in each profile, as verified by the EBSD measurement.

62° . Thus, the coefficient values suggest that the disorientation angle (*angle1*) and the third Rodrigues vector component contribute most strongly to CV1, whereas *near111* and *near100* dominate CV2 (inputs).

In Fig. 11, the boundaries close to the exact twin (i.e., $\Sigma 3$) are colored red and a few boundaries that are not as close, green. The plot shows that, although there is a reasonably strong correlation of 0.6, the relationship between the pair is obviously non-linear and that, within the twin boundary set (red points), there is considerable variation in the CL signal for negligible variation in the input variate.

A weak correlation between the EBIC and the inclination of the grain-boundary plane with respect to the sample surface was found (not shown). One difficulty, however, in understanding possible correlations with the EBIC signals stems from the fact that the EBIC measurements were performed at room temperature, resulting in only shallow minima (by contrast to the CL signals acquired at 8 K). We also considered the relevance of the grain-boundary trace. However, while for the determination of the disorientation of a grain boundary, a small error of $1\text{--}2^\circ$ may be assumed and the corresponding error for the trace angle is much larger (about $5\text{--}10^\circ$). Accordingly, it was not surprising that the trace angle did not exhibit any correlation with either signal. Enhanced insight into this aspect strongly motivates a future effort to acquire three-dimensional EBSD, EBIC, and CL data from the CuInSe_2 layer.

The absence of a strong correlation between the crystallographic properties of a grain boundary (determined by evaluating the EBSD data) with the EBIC/CL data can be explained by the

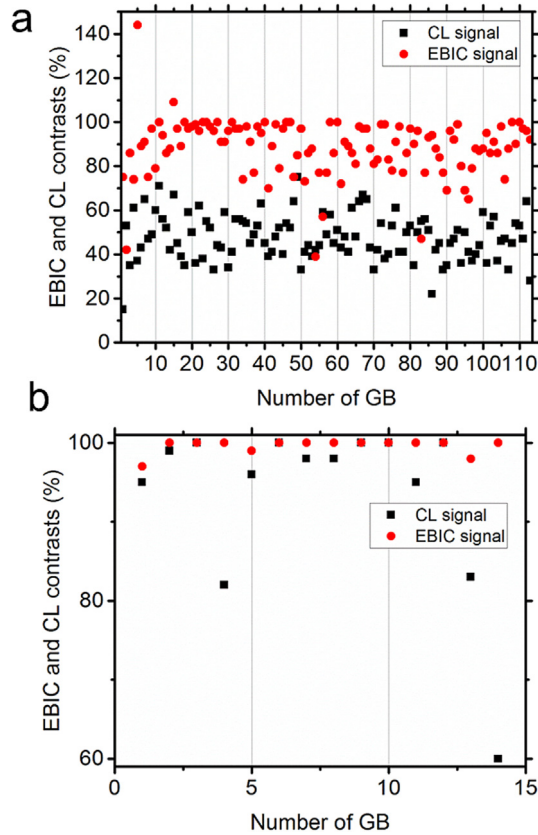


Fig. 10. EBIC and CL signal changes in percent, with respect to the neighboring grains, for the selected 113 random grain boundaries, (a), and 14 ≥ 3 twin boundaries, (b).

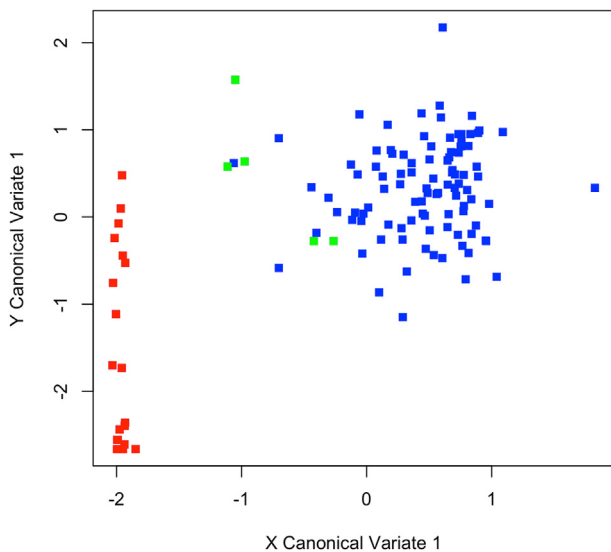


Fig. 11. Plot of the output (vertical) versus the input for the first pair of canonical variates. This shows that the CV1-Y (mostly CL) and CV1-X (mostly *angle1* and *r3*) are moderately correlated (coefficient = 0.6) but that the relationship is clearly non-linear. Points corresponding to twin boundaries are marked in red and near-twin boundaries are in green. (For interpretation of the references to color in this figure legend, the reader is referred to the web version of this article.)

atomic reconstruction mechanism at CuInSe_2 grain boundaries, which has recently been reviewed [4]. This mechanism is based on the fact that CuInSe_2 is a substoichiometric compound, which contains a larger density of Cu vacancies on the corresponding

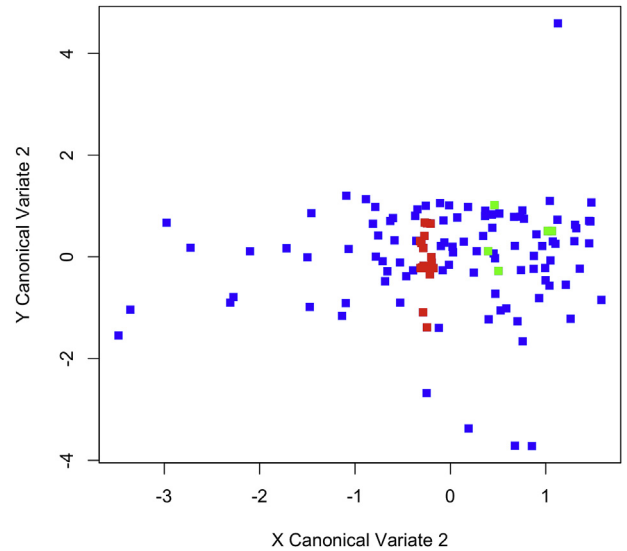


Fig. 12. Plot of the output (vertical) versus the input for the second pair of canonical variates. This shows that the CV2Y (mostly EBIC) and CV2-X (mostly *near111* and *near100*) are negligibly correlated (coefficient = 0.1). Points corresponding to twin boundaries are marked in red and near-twin boundaries are in green; by contrast to CV1, there is nothing that distinguishes the twin boundaries in this plot. (For interpretation of the references to color in this figure legend, the reader is referred to the web version of this article.)

Table 1
Coefficients and loadings for the input group of variables.

Variable	CV1_coeff	CV2_coeff	CV1_loading	CV2_loading
<i>angle1</i> [0–62°]	0.1828995	0.1450985	0.6951312	0.48620127
<i>rf1</i> [<0.414]	4.6249566	–6.3459798	0.9028087	0.29102259
<i>rf2</i> [<0.414]	–1.4191416	0.1769137	0.6650313	0.33580515
<i>rf3</i> [<0.33]	–22.1872932	–9.7370901	0.3058378	0.62226837
<i>near100</i> [<1]	1.0372669	13.4487680	–0.6132051	–0.04266259
<i>near110</i> [<1]	–0.3968742	5.0331263	–0.5884295	–0.02078862
<i>near111</i> [<1]	–2.5063845	13.4979920	0.6401628	0.28911428

Table 2
Coefficients and loadings for the output group of variables.

Variable	CV1_coeff	CV2_coeff	CV1_loading	CV2_loading
CL [<1]	0.05338720	–0.02189764	0.9886071	–0.1505189
EBIC [<1]	0.01188089	0.07803364	0.3794851	0.9251978

lattice sites. Also, a large number of other point defects can be formed, either those related to the matrix elements or those induced by impurity elements such as Na, K, and O, which diffuse from the glass substrate into the CuInSe_2 layer during growth and segregate to (random) grain boundaries. In case of excess charge densities present at grain boundaries, the atomic reconstruction of the neighboring atomic planes adjacent to the grain boundaries effectively reduces these excess charge densities, which influences the collection as well as the recombination of charge carriers considerably. For multicrystalline Si, for which no such reconstruction mechanism is available, the EBIC and CL signals can be expected to correlate much stronger with the crystallographic properties of a grain boundary.

4. Conclusions

The present work provides detailed insight into the crystallographic properties of grain boundaries in CuInSe_2 thin films as well

as their correlations with the electrical and optoelectronic properties. The disorientation angle distribution from a dataset containing 136,000 grain-boundary segments exhibits maxima at 32°, 39°, and 60°, which were assigned to $\Sigma 27a$, $\Sigma 9$, and $\Sigma 3$ grain boundaries. The maximum populations at these disorientations are 8, 68, and 3500 MRD. From EBSD, EBIC, and CL data, all acquired at the same identical position of a CuInSe₂ thin film, correlations of the crystallographic data with the electrical and optoelectronic properties of about 100 random grain boundaries and 14 twin boundaries were analyzed. While most of the random grain boundaries exhibited enhanced recombination with recombination velocities of about 0.5–2 cm/s, most of the twin boundaries do not exhibit a substantial reduction of the EBIC or CL signals. Statistical evaluation by means of CCA of the crystallographic, electrical and optoelectronic data showed no strong correlations of the various quantities. Based on the first pair of canonical variates, the disorientation angle and the third Rodrigues vector component contribute most strongly to the CL signal; from the second pair, there is a weak correlation between *near111* and *near100* and the EBIC signal. The absence of a strong correlation with grain boundary character may be explained by the atomic reconstruction at planar defects in CuInSe₂ thin films, which act as a mechanism to reduce effectively excess charge densities and hence affect substantially the electrical and optoelectronic properties.

Acknowledgements

The authors would like to thank all colleagues at HZB who assisted in producing solar cells and maintaining the electron microscopes. Financial support by the Helmholtz Virtual Institute VH-VI-520 “Microstructure Control for Thin-Film Solar Cells” and by the ONR-MURI program (grant no. N00014-11-0678) is gratefully acknowledged.

References

- [1] P. Jackson, R. Wuerz, D. Hariskos, E. Lotter, W. Witte, M. Powalla, Effects of heavy alkali elements in Cu(In,Ga)Se₂ solar cells with efficiencies up to 22.6%. Phys. Stat. Sol. (RRL), DOI: 10.1002/pssr.201600199 https://www.zsw-bw.de/fileadmin/user_upload/PDFs/Pressemitteilungen/2016/pr09-2016-ZSW-WorldRecordCIGS.pdf (accessed 04.07.16).
- [2] Dr. Philip Jackson, Z.S.W. Stuttgart, Germany, Private Communication.
- [3] U. Rau, K. Taretto, S. Siebentritt, Grain boundaries in Cu(In,Ga)(Se, S)₂ thin-film solar cells, Appl. Phys. A 96 (2009) 221.
- [4] D. Abou-Ras, S.S. Schmidt, N. Schäfer, J. Kavalakkatt, T. Rissom, T. Unold, R. Mainz, A. Weber, T. Kirchartz, E. Simsek Sanli, P.A. van Aken, Q.M. Ramasse, H.-J. Kleebe, D. Azulay, I. Balberg, O. Millo, O. Cojocaru-Mirédin, D. Barragan-Yani, K. Albe, J. Haarstrich, C. Ronning, Compositional and electrical properties of line and planar defects in Cu(In,Ga)Se₂ thin films for solar cells - a review, Phys. Stat. Sol. (RRL) 10 (2016) 363.
- [5] M. Nichterwitz, D. Abou-Ras, K. Sakurai, J. Bundesmann, T. Unold, R. Scheer, H.-W. Schock, Influence of grain boundaries on current collection in Cu(In,Ga)Se₂ thin-film solar cells, Thin Solid Films 517 (2009) 2554.
- [6] M. Müller, D. Abou-Ras, T. Rissom, F. Bertram, J. Christen, Symmetry dependent optoelectronic properties of grain boundaries in polycrystalline Cu(In,Ga)Se₂ thin films, J. Appl. Phys. 115 (2014) 023514.
- [7] W. Lee, J. Chen, B. Chen, J. Chang, T. Sekiguchi, Cathodoluminescence study of dislocation-related luminescence from small-angle grain boundaries in multicrystalline silicon, Appl. Phys. Lett. 94 (2009) 112103.
- [8] C. Kaufmann, A. Neisser, R. Klenk, R. Scheer, Transfer of Cu(In,Ga)Se₂ thin film solar cells to flexible substrates using an in situ process control, Thin Solid Films 480 (2005) 515.
- [9] K.S. Knight, The crystal structures of CuInSe₂ and CuInTe₂, Mat. Res. Bull. 27 (1992) 161.
- [10] S.I. Wright, R.J. Larsen, Extracting twins from orientation imaging microscopy scan data, J. Microsc. 205 (2002) 245.
- [11] G. Rohrer, D. Saylor, B. El Dasher, B. Adams, A. Rollett, P. Wynblatt, The distribution of internal interfaces in polycrystals, Z. Met. 95 (2004) 197.
- [12] D.M. Saylor, B.S. El-Dasher, B.L. Adams, G.S. Rohrer, Measuring the five-parameter grain-boundary distribution from observations of planar sections, Metall. Mater. Trans. A 35 (2004) 1981.
- [13] H. Beladi, G.S. Rohrer, The distribution of grain boundary planes in interstitial free steel, Metall. Mater. Trans. A 44 (2013) 115.
- [14] S.A. Bojarski, M. Stuer, Z. Zhao, P. Bowen, G.S. Rohrer, Influence of Y and La additions on grain growth and the grain-boundary character distribution of alumina, J. Am. Ceram. Soc. 97 (2014) 622.
- [15] S.J. Dillon, M.P. Harmer, G.S. Rohrer, The relative energies of normally and abnormally growing grain boundaries in alumina displaying different complexions, J. Am. Ceram. Soc. 93 (2010) 1796.
- [16] S.J. Dillon, G.S. Rohrer, Characterization of the grain-boundary character and energy distributions of yttria using automated serial sectioning and EBSD in the FIB, J. Am. Ceram. Soc. 92 (2009) 1580.
- [17] C.S. Kim, T.R. Massa, G.S. Rohrer, Interface character distributions in WC–Co composites, J. Am. Ceram. Soc. 91 (2008) 996.
- [18] X. Liu, D. Choi, H. Beladi, N.T. Nuhfer, G.S. Rohrer, K. Barmak, The five-parameter grain boundary character distribution of nanocrystalline tungsten, Scr. Mater. 69 (2013) 413.
- [19] V. Randle, G.S. Rohrer, Y. Hu, Five-parameter grain boundary analysis of a titanium alloy before and after low-temperature annealing, Scr. Mater. 58 (2008) 183.
- [20] V. Randle, G.S. Rohrer, H.M. Miller, M. Coleman, G.T. Owen, Five-parameter grain boundary distribution of commercially grain boundary engineered nickel and copper, Acta Mater. 56 (2008) 2363.
- [21] S. Ratanaphan, Y. Yoon, G.S. Rohrer, The five parameter grain boundary character distribution of polycrystalline silicon, J. Mater. Sci. 49 (2014) 4938.
- [22] http://mimp.materials.cmu.edu/~gr20/stereology/programs_CuInSe2_analysis.zip, (accessed on 11.04.16).
- [23] J. Kavalakkatt, D. Abou-Ras, J. Haarstrich, C. Ronning, M. Nichterwitz, R. Caballero, T. Rissom, T. Unold, R. Scheer, H.W. Schock, Electron-beam-induced current at absorber back surfaces of Cu(In,Ga)Se₂ thin-film solar cells, J. Appl. Phys. 115 (2014), <http://dx.doi.org/10.1063/1.4858393>, 014504-1-10.
- [24] J.D. Jobson, Applied Multivariate Data Analysis, Vol. II, Springer, NewYork, 1992.
- [25] R. Gittins, Canonical Analysis: a Review with Applications in Ecology, Springer, Berlin, 1985.
- [26] D.J. Hand, H. Mannila, P. Smyth, Principles of Data Mining, MIT Press, 2001.
- [27] A.P. Sutton, R.W. Balluffi, Interfaces in Crystalline Materials, Clarendon Press, Oxford, 1995.
- [28] H.J. Bunge, Texture Analysis in Materials Science, Butterworths, London, 1992.
- [29] www.r-project.org, (accessed on 11.04.16).
- [30] <http://cran.r-project.org/package=car>; <http://cran.r-project.org/package=yacca>, (accessed on 11.04.16).
- [31] J.K. Mackenzie, Second paper on statistics associated with the random orientation of cubes, Biometrika 45 (1958) 229.
- [32] W. Bollmann, Crystal Defects and Crystalline Interfaces, Springer, Berlin, 1970.
- [33] V. Randle, The role of the grain boundary plane in cubic polycrystals, Acta Mater. 46 (1997) 1459.
- [34] K. Miyazawa, Y. Iwasaki, K. Ito, Y. Ishida, Combination rule of Σ values at triple junctions in cubic polycrystals, Acta Cryst. A 52 (1996) 787.
- [35] G.S. Rohrer, Grain boundary energy anisotropy: a review, J. Mater. Sci. 46 (2011) 5881.
- [36] H. Yamaguchi, H. Hiramatsu, H. Hosono, T. Mizoguchi, The atomic structure, band gap, and electrostatic potential at the (112)[1-10] twin grain boundary of CuInSe₂, Appl. Phys. Lett. 104 (2014) 153904.
- [37] M. Kawamura, T. Yamada, N. Suyama, A. Yamada, M. Konagai, Grain boundary evaluation of Cu(In_{1-x}Ga_x)Se₂ solar cells, Jpn. J. Appl. Phys. 49 (2010) 062301.
- [38] B.G. Mendis, L. Bowen, Q.Z. Jiang, A contactless method for measuring the recombination velocity of an individual grain boundary in thin-film photovoltaics, Appl. Phys. Lett. 97 (2010) 092112.
- [39] M. Gloeckler, J.R. Sites, W.K. Metzger, Grain-boundary recombination in Cu(In,Ga)Se₂ solar cells, J. Appl. Phys. 98 (2005) 113704.
- [40] N. Tabet, C. Monty, Y. Marfaing, SEM-EBIC investigations of the electrical activity of grain boundaries in germanium, in: J.H. Werner, H.J. Möller, H.P. Strunk (Eds.), Springer Proceedings in Physics, Polycrystalline Semiconductors, 35, Springer, Berlin, 1989, p. 89.